PIXIE data processing at the University of Bergen

TECHNICAL REPORT

N. Østgaard,[1] J. Bjordal,[1] J. Stadsnes,[1] E. Thorsen[1]

Scientific/Technical Report No 1999-05, Dept. of Physics, University of Bergen, ISSN 0803-2696, May 1999

Abstract. The PIXIE instrument onboard the Polar satellite is the first true two-dimensional X-ray camera ever flown in space. Due to the highly elliptical orbit (1.8 x 9 R_E) the PIXIE camera provides global images of the X-ray aurora during an apogee pass for about 12 hours and during a perigee pass for about 40 minutes. Unexpectedly low operational temperatures for the camera electronics, below -10˚ C, has significantly complicated the image processing and correction routines as well as the interpretation of the energy spectral information from the instrument. A complex correction scheme has been established in order to correct for these errors. In this paper we describe in detail how this scheme has been put together and how it works. We also present some results, which make us believe that all the different sources of errors have been taken into account. Restricted to periods of analogue electronics temperature below -10˚ C, we are now able to provide X-ray images and X-ray spectra with a spatial resolution mainly determined by the geometry of the camera and statistical error due to the count rates of the genuine auroral X rays. The data processing described in this paper are now used by the PIXIE group at the University of Bergen. This paper is a detailed description of the data processing and we will consider publishing a shorter version for a broader public.

1. Introduction

The Polar Ionospheric X-ray Imaging Experiment (PIXIE) onboard the Polar satellite is the first true two-dimensional X-ray imager which provides global images of the auroral X-ray bremsstrahlung generated by precipitating energetic electrons seen during substorms. Even though the probability of generating an X-ray photon from a decelerating electron in the atmosphere increases as a function of the initial electron energy, a 200 keV electron only deposits 0.5% of its energy as X rays [Berger and Seltzer, 1972]. Nevertheless these measurements provide the possibility to study the global energetic electron precipitation, even in the sunlit area. Depending on the properness of the data-processing regarding statistical errors, spatial and temporal calibration of the PIXIE instrument the X-ray images can be an important tool in increasing our knowledge about the global behaviour of the energetic electron precipitation into the ionosphere, both statistically and during substorms and storms. This paper describes the PIXIE data processing developed and used at the University of Bergen.

1.1. Instrument design

The instrument is a pinhole camera with four stacked multiwire proportional counters as detecting elements. Two detectors are in the front chamber, which contains a 1.1 atm Ar/CO_2 mixture, has a 0.1 mm Be entrance window, and is sensitive to X-ray photons from about 2 to 10 keV. The rear chamber, with a 2 atm Xe/CO_2 mixture and a 2 mm Be window, contains the other two detectors and covers the energy range from about 10 keV to about 60 keV. Generally the photons are stopped by photoelectric absorption in the detector gas. The photon energy is revealed by the amplitude of the anode signal, and corresponding induced signals in the surrounding cathode wires provide the X and Y positions of the interaction and is read out through a graded density wire structure [Gilvin et al., 1981]. A schematic of the camera is shown in the top panel of Figure 1. The location of the Beryllium windows, cathodes and anodes are indicated for both the front and the rear chambers. Details are provided in Imhof et al. [1995].

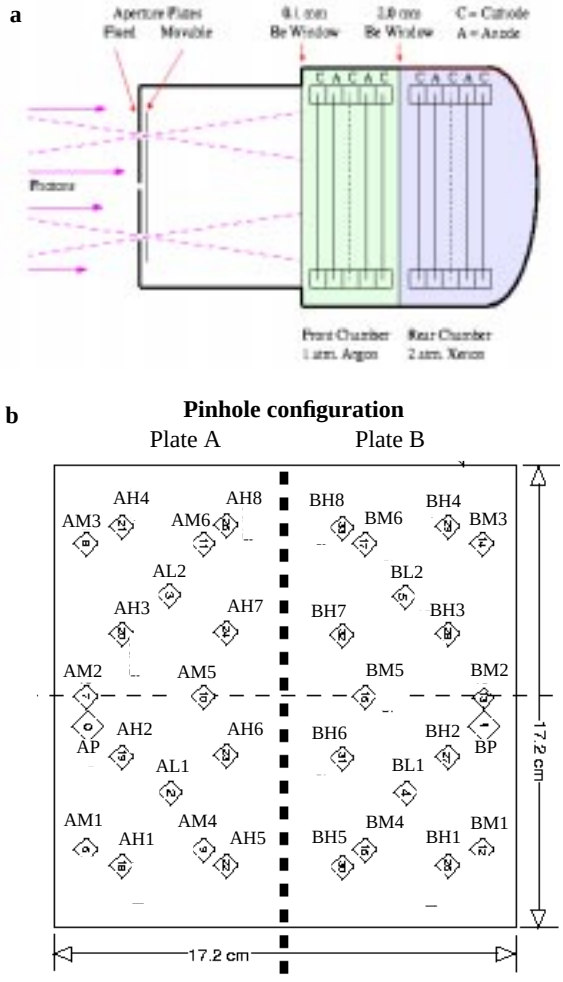

Figure 1. Schematics of the PIXIE camera. (a) The instrument from a side. (b) The different pinhole configuration, AP + BP: 2 x 1 perigee configuration, AH(1:8) + BH(1:8): 2 x 8 apogee configuration, AM (BM) and AL (BL) are intermediate configurations.

[1]Department of Physics, University of Bergen, Bergen, Norway.

At low altitudes (perigee) PIXIE operates with essentially one common pinhole for the four detectors. Polar is in an 1.8 x 9 R_E orbit and to utilize the detector area effectively, the pinhole configuration may be changed from the perigee configuration to 4, 12, or 16 open pinholes depending upon the altitude. The pinhole configuration is set by one fixed plate in front with pinholes as shown in Figure 1b and two moveable pinhole plates behind the front plate, plate A to the left and plate B to the right. There is also a curtain from the pinholes to the front of the detector separating the instrument in two sections, A and B. By moving the plates in a specific position two calibration sources above each halves of the detector can be used for periodical energy calibration. [for further details see Imhof et al., 1995].

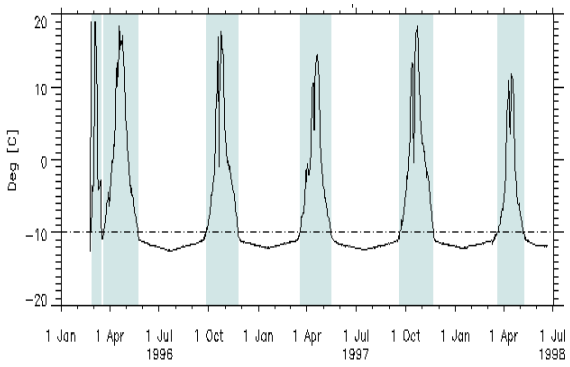

Figure 2. Temperature in the analogue electronics throughout the flight.

The graded density position read-out system has some inherent non linearities. To correct for these a look-up table was included in the instrument electronics in order to linearize the position coordinates and thereby allow the internal 10 bits position signal to be compressed to 8 bits in the telemetry. The sealed multiwire proportional chambers were expected to show some long term deterioration effects due to loss of detector gas, internal contamination, or exposure to harsh radiation conditions in space. Variable high voltage settings and discriminator levels controlled by ground command are included to deal with this. To avoid damage due to high radiation doses, PIXIE is turned off during passage through the radiation belts. This provides an effective operational time per 18 hour orbit of about 12 hours during apogee passes and about 40 minutes during perigee passes.

1.2. Complications during Operations

The operational temperature of the instrument electronics was expected to be slightly below room temperature. However, in orbit it was found that the temperature most of the time was below -10˚C, which was about 25˚C lower than anticipated. The temperature rises to about 15˚C for a short time around the biannual flip manoeuvre of the satellite as shown in Figure 2. This change in operational temperature has introduced unknown gain shifts and signal offsets in the instrument electronics. The main effects of this are:

1. The position coordinate linearization by the look-up table works more like a ‘scrambler’ rather than a correction procedure. The position corrections routines now have to be energy and temperature dependent and each wire layer (cathode) now behaves differently.

2. The instrument energy calibrations taken at near room temperatures are no longer valid.

Additional problems which appeared during flight:

3. The front chamber (the low energy section of the instrument) developed an intermittent high voltage supply problem, which is resolved by duty cycling the high voltage supply. In the early stage this instrument section could be operated at less than 10% duty cycle, but later one has obtained up to 80% duty cycle, which is quite satisfactory.

4. As mentioned the pinhole configuration is changed by moving plate A and plate B. Some months after launch plate B developed strong tendencies to get stuck. Since then this plate has been operated as little as possible. It has for extended time periods been left in a fixed convenient position, and calibration runs have been avoided for this half of the camera (which would have required movement of plate B).

5. A gradual increase of the gain in the front chamber which is interupted by a smaller decrease during each biannual flip of the satellite.

Due to these unpredictable changes to the operation of the camera a complex procedure had to be developed and applied in order to correct for all the errors introduced in the observations. In this paper we describe in detail how this scheme has been put together and how it works. We also present some results, which make us believe that all the different sources of errors have been taken into account. Since PIXIE analogue electronics temperatures spend most of its time below -10˚C we have concentrated on developing a correction procedure for this temperature range, and we are at present able to provide X-ray images and X-ray spectra with a spatial resolution only dependent on the geometry of the camera and statistical error due to the count rates of the auroral X rays.

1.3. The Main Steps in the Image Processing

To produce calibrated images corrected for the non-linear effects our procedure goes through the following steps.

1. For the time interval of interest raw energy and position data are binned into 256 x 256 pixels in 5 different energy bands for each of the four layer. Dead time correction (both an electronic dead time and the limitation of the buffer size) is applied on each X-ray event.

2. The energy efficiency correction for the specified layer is applied to each event.

3. After accumulating events for the specified time interval the background is subtracted. For this purpose we use a 3 by 3 pixels smoothed background matrix sampled for each layer in 5 different energy bands.

4. An algorithm is applied to remove the small scale non-linear effects in the image. The correction factors are based on non-smoothed background matrix for the chosen layer and energy band.

5. Linear large scale correction factors are applied in order to make the distance between sub-images equal the distance between the pinholes. By sub-images we mean the images of auroral ovals underneath each open pinhole. Different large scale factors are used for each layer and energy band.

6. Superimposing sub-images. Pixels close to the edges and below the main front structures of the camera are not used. To provide an exact superposition and keep track of the pixel corresponding to the pinhole the center pixel of the focal plane has to be defined. This is probably the most crucial parameter to get the right projection down on earth.

7. Smooth the image according to the spatial resolution given by the geometry of the detector. Statistic errors are also calculated based on the original counting rate of auroral X rays.

8. Finally the image is projected down on earth at 100 km altitude.

2. Count Rate Corrections

The telemetry rate for PIXIE is limited to about 135 events per second. The instrument electronics includes an elaborate veto system to reject non-auroral events recorded by the detector to prevent non-interesting events from clogging the telemetry. The electronics keeps counts of the number of events rejected and of the number of "good events". These are telemetered to the ground once per half telemetry data frame, i.e., 4.6 s. To obtain the correct X-ray fluxes at the satellite the rate of telemetered good events has to be corrected for dead times of the detector and the electronics, the limited capacity of the telemetry and the effects of the telemetry buffer.

The dead time of the detector is negligible in comparison to electronic dead times. The electronics spend 85 and 15 microseconds, respectively, to process each good event and rejected event. The ratio of telemetered good events to recorded good events if only electronic dead time is taken into account as shown by the dotted curve in Figure 3. The actual ratio is shown by the solid line. The difference between the curves is caused by the limited telemetry rate and the 4 events deep buffer in the telemetry. To compute the exact ratio all events from all layers have to be read, so to reduce computing time an analytical approximation is used for the dead time correction, as described in appendix.

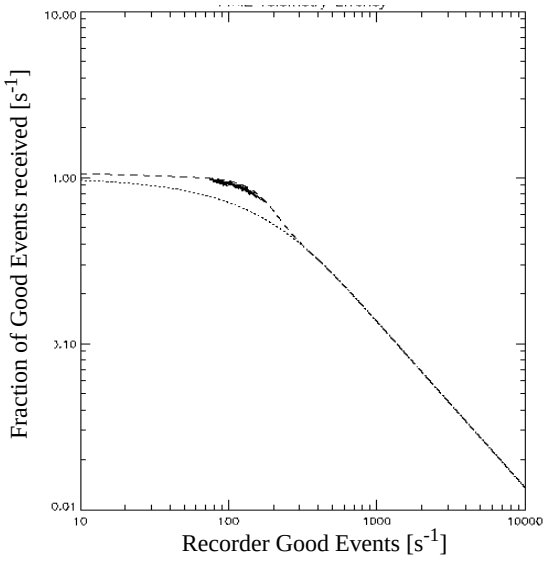

Figure 3. Fraction of telemetered (received) counts versus recorded good event rate. Measured good event rate is shown by solid line. Analytical formula, F_A (12) is shown by dotted line. Total fraction F_T (14) is shown by dashed line.

3. Detection Efficiency and Energy Calibration

The detection efficiency function for each layer has been calculated by taking into account the attenuation of the incoming X-ray flux in different regions of the detector. 20 different regions of the detector have been identified with density, ρ, attenuation coefficient, μ, and depth, x, see Table 1 and Table 2. The attenuation coefficient, μ, is given by tables for the different materials. Applying (1) to each of these regions and sum together the total absorption (A_T) was established for each detector layer.

Table 1. The specified regions in the detector used to calculate the different attenuation.

i	Material	Depth, x_i [mm]
1	1st Be - window	
2	2nd Be - window	0.1524
3	Ar/CO_2 - (90/10) gas	4.0
4	1st cathode layer	0.030
5	Ar/CO_2 - (90/10) gas	5.5
6	1st anode layer	0.0125
7	Ar/CO_2 - (90/10) gas	5.5
8	2nd cathode layer	0.050
9	Ar/CO_2 - (90/10) gas	5.5
10	2nd anode layer	0.0125
11	Ar/CO_2 - (90/10) gas	5.5
12	3rd cathode layer	0.030
13	Ar/CO_2 - (90/10) gas	23.9
14	3rd Be - window	2.286
15	Xn/CO_2 - (90/10) gas	5.8
16	4th cathode layer	0.030
17	Xn/CO_2 - (90/10) gas	5.5
18	3rd anode layer	0.0125
19	Xn/CO_2 - (90/10) gas	5.5
20	5th cathode layer	0.050

Table 2. Mean density, ρ in the different regions of the detector. For the wire layers a weighted density value is used.

Material	ρ [g/cm^2]
Beryllium	0.1845
Gold (Au) plated	
Tungsten (W) wires	19.3
Argon	0.0017832
Xenon	0.005897
CO_2	0.0019769

$$A_T = \sum_{i=0}^{19} (1 - \exp(\mu_i \cdot \rho_i \cdot x_i)) \quad (1)$$

Any difference between the efficiency corrected spectra from the two detector layers in the same chamber would indicate a change in pressure or a gas leakage. So far the gas leakage for PIXIE has been negligible. The resulting efficiency functions for the four layers are shown in Figure 4. It could be mentioned that the image data so far have been taken essentially from layers 1 and 3 for which of the correction routines mentioned below have been developed most accurately.

In PIXIE the photon energies are digitized into 64 energy channels for each layer. Energy calibration is performed by two internal X-ray calibration sources, one at 5.895 keV for anodes 1 and 2, and another at 22.1 keV for anodes 3 and 4.

To define the peaks of the calibration source for each layer the counts are accumulated separately by dividing each section of the focal plane in 8 squares. But in order to avoid edge effects only data obtained in the two squares nearest to the center of the detector are used for the energy calibration. For calibration the pinhole

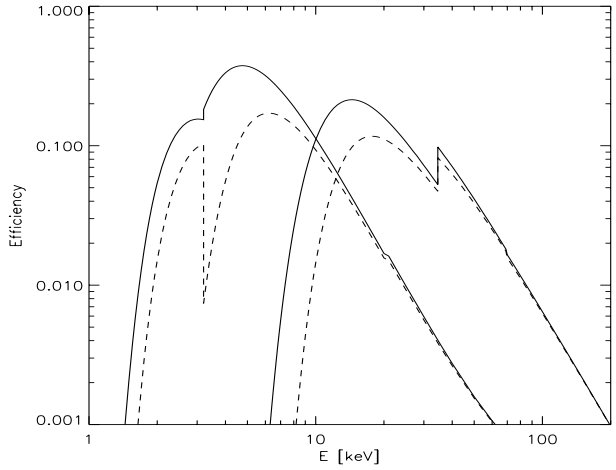

Figure 4. Energy efficiency function. Layer 1 and layer 3 are shown by solid lines. Layer 2 and layer 4 are shown by dashed lines. The K-line for Argon can be seen in efficiency function for layer 1 and 2 to the left, and the K-line for Xenon is seen in the layer 3 and 4 function to the right.

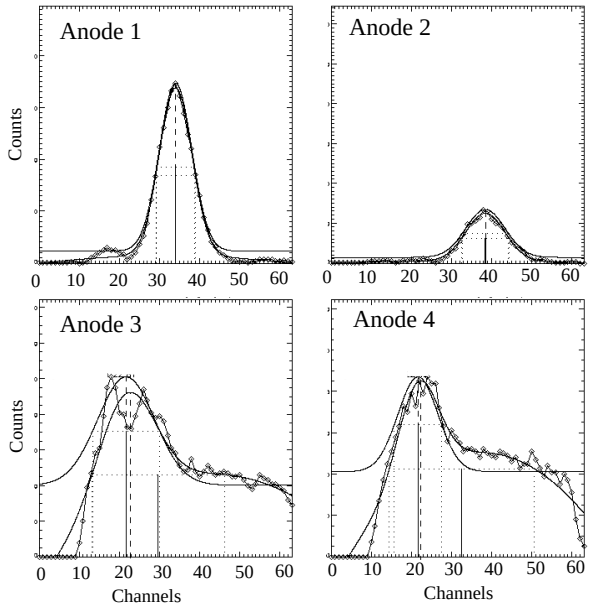

Figure 5. Determination of the channel number where the calibration source is detected for the different layers. Calibration run for May 14, 1997.

plates are moved to a position where all pinholes are closed and the two calibration sources are uncovered. Since plate B developed a tendency to get stuck no calibrations have been performed on that side of the instrument since June 1996. For anode 1 and 2 the counts within the two central squares under plate B are used as a measure of the background radiation and subtracted to obtain a more clear calibration signal. For anode 3 and 4 this could not be done, as the calibration source is too weak. The peak channel of the spectrum in each anode is determined by taking a gaussian fit

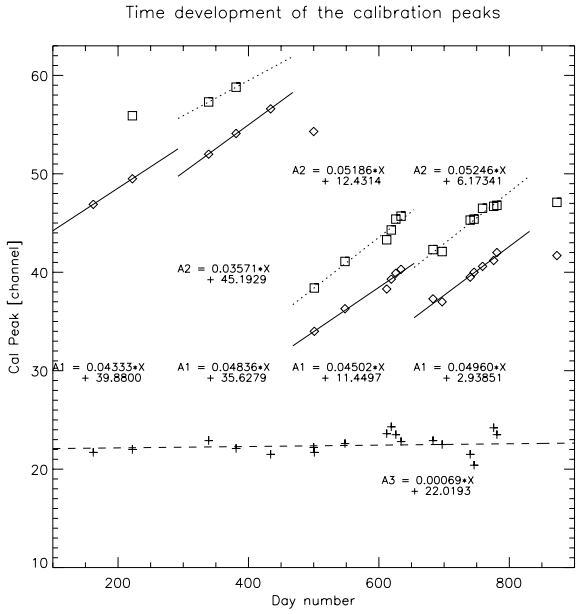

Figure 6. Time development of the channel number where the calibration source is detected for the different layers.

to the measurements. Figure 5 shows, as an example, data from a calibration run (May 14, 1997). In layer 1 the Argon escape peak is seen at 2.9 keV below the calibration peak, providing two calibration points and thus enabling determination of both the gain and offset for this layer.

In layers 3 and 4 the Xenon gas mixture creates a double peak in the spectrum for 22.1 keV, making the energy resolution quite poor. Both peaks are here taken into account to determine the position of the calibration peak.

The energy calibrations have revealed an unexpected gain drift in the front chamber. Figure 6 shows the position of the spectral peak, P_C, in layers 1, 2, and 3, versus time (day number since 1 Jan. 1996, d_N), and we see an approximately linear relation between P_C and d_N for each layer. The linear relation is given by (2) and the coefficients for layer 1 and 2 are given in Table 3. For layer 3 and layer 4 the spectral peak varies very slowly with time.

$$P_C = A \cdot d_N + B \tag{2}$$

Table 3. The coefficient for the linear relation between peak channel number and day number.

Days number	Layer 1		Layer 2	
	A	B	A	B
100 - 292	0.0433	39.8800		
292 - 468	0.0484	35.6279	0.0357	45.1929
468 - 654	0.0450	11.4497	0.0519	12.4314
654 - 831	0.0496	2.9385	0.0525	6.1734

By examining the Argon escape peak for layer 1 and 2 there is also found to be a linear relation between the peak of the calibration source, P_C and the offset, O, i.e. the channel number for 0 keV. For layer 1 and 2 this relation is given by (3) and (4):

$$O_1 = 0.279 \cdot P_{C1} - 6.59 \tag{3}$$

$$O_2 = 0.490 \cdot P_{C2} - 18.4 \quad (4)$$

For the rear chamber our calibration source has only one X-ray line. To obtain an estimate of the offset in the rear chamber we based our reasoning on the fact that in general an X-ray bremsstrahlung spectrum has to be monotonously decreasing towards higher energies. Furthermore, an eventual hinging point (i.e., the transition from one dominating e-folding energy to another) shall not necessarily be at the intersection of the ranges of anode 1 and anode 3. By applying a non-zero offset to the energy spectrum of anode 3 we found it possible to a large extent to comply with these constraints. We have inspected spectra from a number of intense auroral X-ray events spread over 18 months of the flight, and applied these requirements. For 7 strong X-ray events we found that an offset of 3 channels (i.e., channel 3 corresponds to 0 keV) gave the best results. We therefore use this as our best estimate of the offset in anode 3. Figure 7 shows an example from February 9, 1997 of the impact of applying the offset. Both the auroral X-ray spectrum and the background spectrum are folded through the energy efficiency function (Figure 4). From this study we also found that the fluorescence peak (at about 30 keV) and background noise in the Xenon gas tend to dominate the count rates above channel 22 in anode 3, but by integrating from channel 10 to 15 and from channel 16 to 21 we still get spectral information from anode 3 with statistical significance.

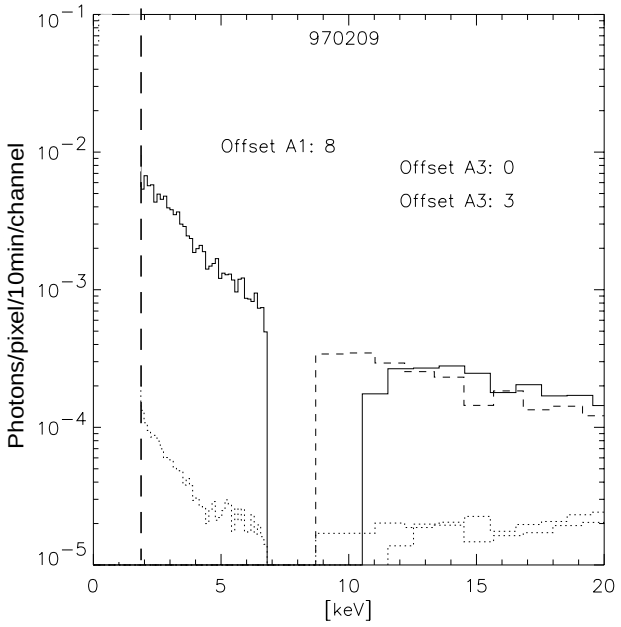

Figure 7. Energy spectrum of auroral X rays (background subtracted) from February 9, 1997. For anode 1 an offset of 8 channels is applied. For anode 3 the solid line shows the spectrum with no offset applied and dashed line shows the spectrum when an offset of 3 channels is used. The dotted lines show the subtracted background spectra in the two energy ranges. For anode 3 the two dotted lines correspond to the different offsets applied. Both the auroral X-ray spectrum and the background spectrum are folded through the energy efficiency function shown in Figure 4.

When both the gain, i.e. the peak position of the calibration source and the offset dependence on time are found, we have established the input parameters needed to fold every dead time corrected X-ray event through the energy efficiency function.

4. Accumulation and Identification of Background Count Rates

In spite of the background suppression circuits in the PIXIE instrument there is a need for further background subtraction during the image processing in order to obtain the best possible images of the X-ray aurora. Our procedure has been to collect typical samples of the background and subtract these from the raw images. As indicated above both the energy and position data from PIXIE exhibits temperature and temporal variations. Typical samples of the background have thus been collected at several times during the operation of PIXIE and binned into several energy bands. Since PIXIE spend most of its time at low temperatures, the background samples so far are only taken during such conditions.

For a time interval to be classified as background interval we required:

1. Analogue electronic temperature is below -10° C.
2. No auroral X rays nor celestial X rays are visible.
3. Satellite at radial distances greater than 6 R_E.

As the position signal (in both x and y) is given by (5).

$$x_i = \frac{q_B + dq_B}{q_A + dq_A + q_B + dq_B + d(q_A + q_B)} \quad (5)$$

where q is charge deposited at the wires, read out as the two signals A and B, we know that the gain shifts and/or the offsets will effect the read-out system differently for different energies. If dq_b and dq_a are negative the low energy X rays will tend to be observed closer to the edges than the more energetic X rays. By inspecting the background matrices for two different energy bands in layer 1, this effect is clearly seen in Figure 8 and indicates that the offsets are both negative. Aware of this we have sampled background matrices for different periods of time and for 5 different energy bands in each layer. The separation in 5 energy bands, i.e. ten channels in each band was chosen in order to improve the statistics in each energy band. As the background count rate increases significantly when the front chamber is turned off, as is the case when the veto system is turned off in the front chamber we have sampled background for layer 3 and layer 4 in 5 different energy bands both for times when front chamber is on and off. For each time period of background sampling we obtain 4 layers x 5 energy band + 2 layers x 5 energy bands = 30 background matrices. As we found that the fluorescence peak and background noise in the rear chamber to dominate the count rates in anode 3 above channel 22, we have sampled the background for this anode in two energy bands, channels 10 through 15 and channels 16 through 21. So far we have sampled 7 sets of background matrices as listed in Table 4. These background matrices are used for two different purposes, to subtract the background and as input for the non linear correction algorithm described in Section 5.. To minimize the statistical fluctuations in our background subtraction we have smoothed the background matrices used for this purpose 3 by 3 pixels.

5. Correction of the Non-linear Effects

The striped or checked patterns seen in the background matrices (Figure 8) are assumed to reflect the failure of the built-in

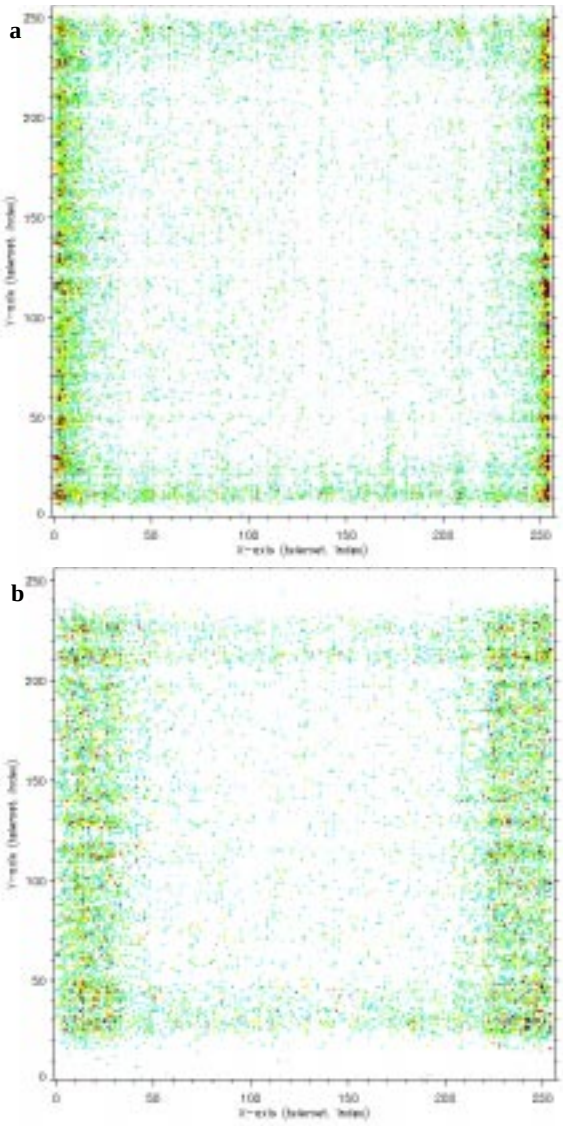

Figure 8. Background sampled from November 26, 28 and 29, 1997. (a) Layer 1 in energy channels 10-19. (b) Layer 1 in the energy channels from 50-63. Both panels show 2.4 hours of background normalized to counts per 10 min.

Table 4. Times of background sampling.

Hours of background sampling (In parenthesis: Front Chamber: OFF)				
Time	Layer 1	Layer 2	Layer 3	Layer 4
05.12.96 - 02.01.97	2	2	2 (7)	2 (7)
20-23.05.97	2.5	~2.5	2.5 (3)	2.0 (3)
03-05.08.97	2.3	2.3	2.3 (2.5)	2.3 (2.5)
26-29.11.97	2.4	2.4	2.4 (3.5)	2.4 (3.5)
20-23.05.97	2.5	~2.5	2.5 (3)	2.0 (3)
03-05.08.97	2.3	2.3	2.3 (2.5)	2.3 (2.5)
26-29.11.97	2.4	2.4	2.4 (3.5)	2.4 (3.5)

look-up tables to correct for the inherent non-linearities of the graded density cathodes. The underlying cause is the temperature drift in the electronics. Below we present the arguments for assuming that this pattern is similar to what the auroral X rays will produce, and thus justify that the background matrices may be used to correct for the non-linearities in the X-ray images.

5.1. Sources of Background Radiation

As background radiation we consider all radiation which are not X rays produced by precipitating electrons in the atmosphere. There are at least three sources for this background radiation.

1. X-ray bremsstrahlung produced when energetic electrons strike the structures surrounding the chambers. These X-ray photons will probably enter the detector chambers almost isotropically, with some preferences of radiation from the sides and the rear due to the location of the surrounding structures.
2. Cosmic X rays coming in through the pinholes. These X rays will be detected during apogee passes when the Earth does not cover the whole field of view of PIXIE.
3. Minimum ionizing particles passing through the chambers and avoiding the veto system.

Minimum ionizing particles will be detected at some false and 'average' positions as they have long tracks of ionization. As these particles deposit their energy by ionizing all their way through the detector, the position mostly depends on the entering angle of the particle. As the anti-coincident system will veto the minimum ionizing particles entering two layers, the energy deposition by the particles will be seen most clearly near the edges in each layer and most clearly in layer 1 and layer 4. This is observed in all our background images.

As can be seen from Figure 7 the slope of the background spectrum (i.e., the dotted line) from anode 1 is monotonously decreasing with increasing energies. This indicates a significant contribution of X rays in the background, as minimum ionizing particles should give a spectrum falling off at low energies. However, the anode 3 background spectrum (Figure 7, dotted line) increases with increasing energy indicating a background mainly generated by particles. From this we conclude that the background in anode 1 is composed mainly by X rays, partly produced in the surrounding structures of the camera and partly by cosmic X rays. Furthermore this indicates that the checked pattern of the background is similar to the checked pattern of auroral X rays. This has also been examined by adding many auroral events and correlating the patterns with the background patterns. Even in anode 3 where the background is generated mainly by particles, we find the correlation to be good. This means that the information of non-linear effects in the background can be used to correct for the non-linear effects seen in the auroral X-ray images for both the front chamber and the rear chamber.

5.2. Correction Algorithm: Small Scale Factors

By inspecting the (not smoothed) background matrices we notice that the non-linear effects appear as vertical and horizontal lines in the focal plane, indicating that the correction can be provided separately along x and y. Based on this we calculate the small scale factors by summing all y (x) values along the x (y) and then normalize each sum by the average of the +/- 5 sum columns (rows) as given by (6) and (7). Small scale factors are calculated along x and y for each layer in 5 different energy bands.

$$C_i = \frac{\sum_{j=0}^{255} X_{ij}}{\left(\sum_{(n=i-5)}^{i+5} \sum_{(j=0)}^{255} X_{nj} \right) / 11.} \quad (6)$$

$$C_j = \frac{\sum_{i=0}^{255} X_{ij}}{\left(\sum_{(i=0)}^{255} \sum_{(n=j-5)}^{j+5} X_{in} \right) / 11.} \quad (7)$$

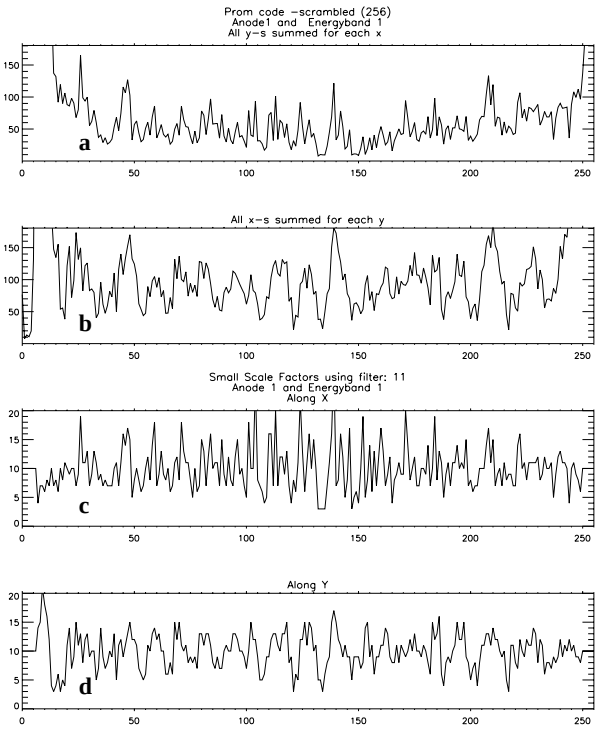

Figure 9. (a-b) The column (row) sum of along x-axis (y-axis). (c-d) the small scale factors along x and y, calculated by (6) and (7).

In the two upper panels of Figure 9 the column and row sums along x and y are shown and strong edge effects can be seen. The column sums rise to very large values, and the row sums increase and then go to near zero. The two lower panels show the small scale factors for layer 1 in energy band 1 (channel 10-19). To avoid the edge effects mentioned above, the factors for the 10 pixels near the edges are set to 1.0. It will later be shown that we are not using data from these pixels when we superimpose the sub-images to get the final image. As we are going to use the small scale factors both for scaling the count rates and widening/ narrowing the pixel size we must require the sum of small scale factors both along x and y to be 2559 (8).

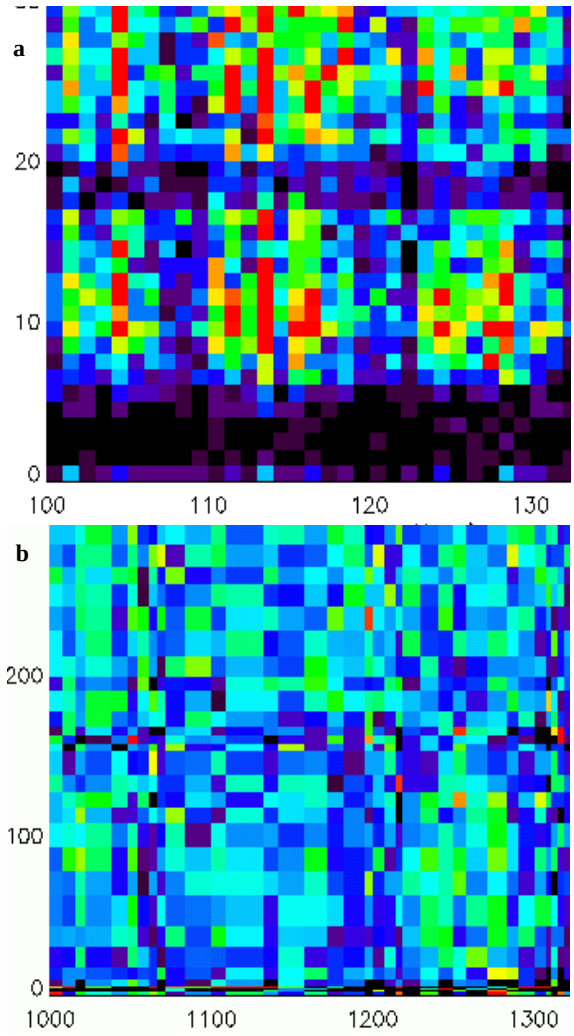

Figure 10. (a) A part of a 2560 x 2560 matrix of background X rays (100:130, 0:30 pixels).(b) The same part of the matrix after widening some and narrowing other pixels

$$\sum_{i=0}^{255} C_i = \sum_{j=0}^{255} C_j = 2559 \quad (8)$$

The small scale factors are now used to redistribute the auroral X-ray counts in each pixel row/column to correct for non-linearities in the focal plane. Each column of auroral X rays in the x-dimension (and each row in the y-dimension) are scaled by multiplying by the inverse of the correction factor, see (9). The widening and narrowing of the pixels are provided by putting these scaled values into 10 times C_i columns (rows) in a 2560 times 2560 matrix. If the small scale factor is found to be 15, the counts in one pixel row are placed in 15 new pixel rows and the count rate in each new row is divided by 15. The same procedure is applied along the pixel columns (along the x-dimension)

$$X'_i = \frac{\sum_{i=0}^{255} X_{ij}}{C_i} \quad (9)$$

Figure 10 shows the result of using this procedure for a small part of the large 2560 times 2560 matrix.

6. Large Scale Factors

After redistributing the auroral X-ray counts by applying the small scale factors we need to make sure that the separation between auroral features in the focal plane is consistent with the separation between the pinholes. For this purpose we have assumed that the matrices corrected for small-scale non-linearities can be linearly adjusted by a constant factor for x and y separately, giving us the exact pixel to mm conversion factors. Large scale factors are calculated for each set of background sample used for the small scale correction. Sub-images of auroral ovals observed close in time to a background sample are spatially correlated to the pinhole positions to determine these large scale factors. Similar to the background sampling and the small scale correction, large scale factors are found for each layer in 5 different energy bands. In Figure 11 we have shown the correlation results for one event along x for layer 1 energy band 3 (channel 30-39).

The results for three times of background sampling are listed in Table 5 below. For all the layers we find an energy dependence consistent with our assumptions of negative offsets in the read-out system from the cathodes. Significant time variations are only seen in the front layers (1 and 2) in accordance with the findings regarding the peak position of the calibration source.

Table 5. Large scale factors for layers and energy bands for three different background samples.

	X			Y		
Layer E-band	Dec. 96	May 97	Aug. 97	Dec. 96	May 97	Aug. 97
L1 EB2	0.90	0.89	0.88	0.96	0.95	0.96
L1 EB3	0.93	0.91	0.915	0.97	0.98	0.975
L1 EB4	0.95	0.93	0.94	0.98	0.98	0.995
L1 EB5	0.98	1.00	0.98	0.995	1.00	1.04
L2 EB2	0.93	0.94	0.91	0.96	0.93	0.97
L2 EB3	0.98	0.96	0.94	0.99	0.95	0.94
L2 EB4	1.00	0.99	0.985	1.00	0.98	1.005
L2 EB5	1.01	1.02	1.01	1.02	1.02	1.02
L3 EB1	0.96	0.96	0.95	0.93	0.92	0.935
L3 EB2	0.98	0.98	0.98	0.96	0.96	0.96
L4 EB1	0.83	0.83	0.83	0.91	0.91	0.91
L4 EB2	1.0	1.0	1.0	1.0	1.0	1.0

7. Center Pixel of the Focal Plane

To provide an accurate superposing of the sub-images and to project the superimposed image properly down on earth, we need to know accurately the center pixel of the focal plane. This is the most crucial parameter of the projection routine.

The values of the center pixels of the four layers can be obtained by a two step procedure:

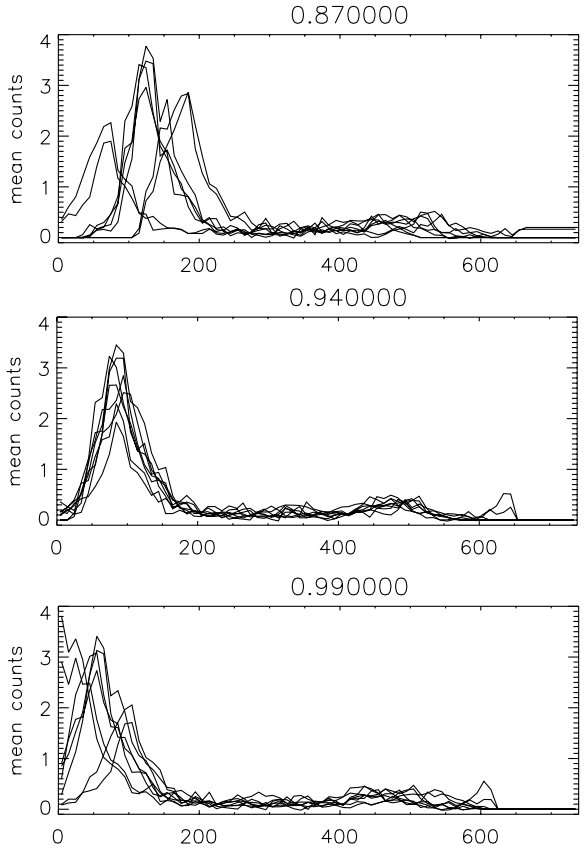

Figure 11. The correlation in the x-dimension using different large scale factors, C_L, assuming that the ratio of pixels to mm on a large scale can be expressed as a constant, C_L times 256/172. For this event maximum correlation (0.88) was found for C_L=0.94 (middle panel).

1. Determine the center pixel by comparing the predicted and observed locations of the celestial X-ray source Circinus X-1 which enters the collimator at slant angles through the pinholes.
2. Claiming bright spots of auroral X rays observed in both the front chamber and the rear chamber to overlay.

7.1. Center Pixel Values from Circinus X-1

The position of the neutron-star binary Circinus X-1 X-ray source is accurately known. By comparing the nominal and observed locations of its image an absolute position calibration is obtained for center pixels of the first two detector layers. Due to the softness of the spectrum from Circinus X-1 the method can only be applied to the front chamber.

The determination of the position of the image of Circinus X-1 is based on a centroid calculation of the detected count rates. Such calculations work quite well in regions of flat background. However, when the image of Circinus X-1 is located on a large gradient background, as is the case near the edge of the detector in the X direction, the peak of the centroid will be shifted towards the edge. This probably is the reason why calculations of center values along X give quite different values depending on the flip mode of the satellite. While the focal plane images of Circinus X-1 may appear at any Y position, they appear either near the edge or near the center of the detector in the X direction. This is illustrated in

Figure 13a. During the summer flip mode of the satellite the images appear near the edge of the detector on the A side and near the center of the detector on the B side, and vice versa during the winter flip mode.

To utilize the information from the Circinus X-1 data to establish our best estimates of the center value in both X and Y and exclude the uncertainties mentioned above, we have to proceed differently for the two dimensions. We perform the Circinus X-1 position calibration for each of the five energy bands for both X and Y and for the two different flip modes of the satellite. We only use Circinus X-1 images in the central parts of the focal plane to establish their X positions in order to avoid errors introduced by steep gradients in the background near the edges. This implies that we need values from both flip modes to determine the X center value. Along Y, the calculation of centroids can be carried out on a uniform background, giving rather precise determination of the center value for each flip mode separately.

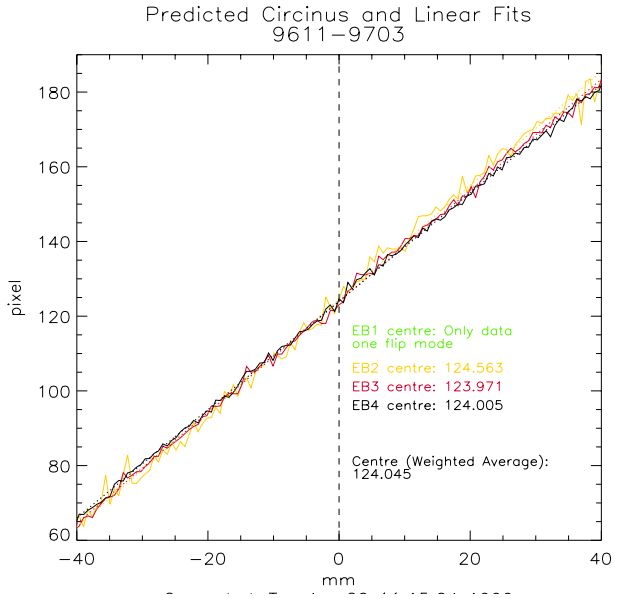

Figure 12. center value in Y derived from Circinus X-1 prediction versus measured for one flip mode: Nov. 96 - Mars 97

By assuming the Y positions of the Circinus X-1 images for two flip positions (during analogue temperature below -10˚C) to be mirror images around the center of the focal plane, the center pixel in Y is found. We get separate values for the different energy bands, and the values are consistent with our finding of negative offsets in the amplifiers for the energy signal, which should be most significant for low energies. By assuming the 'true' center values to be the intersection of all energy bands, as shown in Figure 12, we get the values listed in Table 6. We interpret these two values to be the 'true' centres along Y for each flip mode.

Table 6. center values in y, derived from measured and predicted position of Circinus X-1 for the two flip modes.

	Y center values		
	Nov. 96-Mar. 97	May 97-Sep. 97	Mean
L1	124.045	125.182	124.6

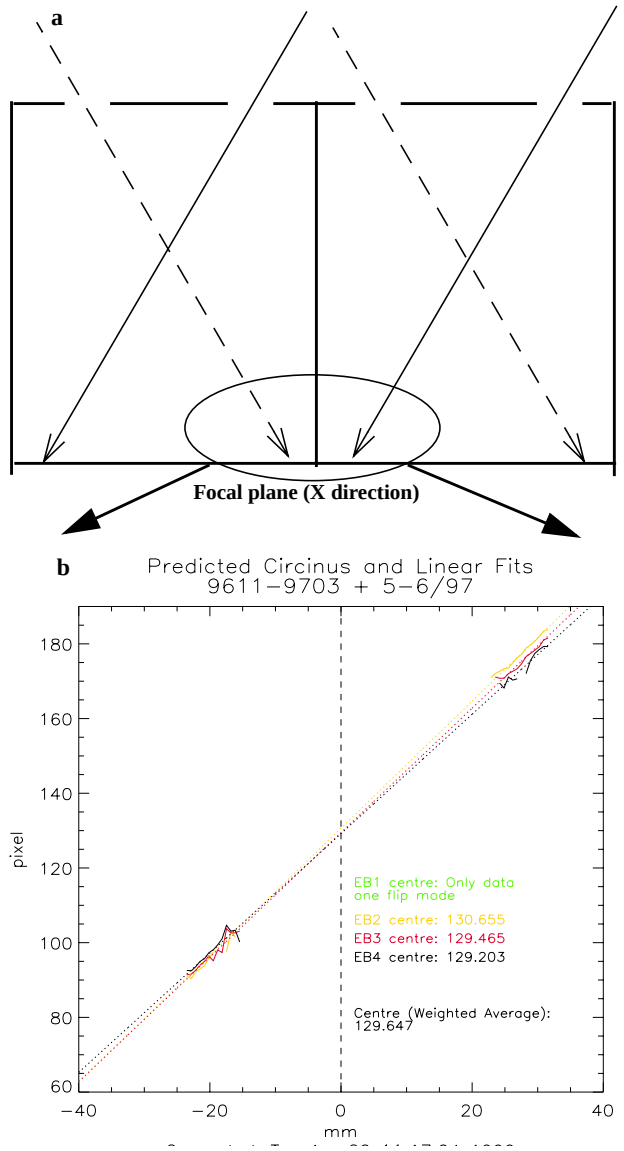

Figure 13. (a) A sketch of where the Circinus X-1 images are located in the focal plane during the two flip modes, solid lines and dashed lines respectively. (b) Plot of pixel values (X) of the Circinus X-1 images versus predicted positions. Points on the left side are from one flip mode, those in the right side from the other. Only the central area of the focal plane is shown.

plane. In both flip modes one column of images will appear near the edge of the detector, in the region where the background level shows a strong gradient. Assuming symmetry in the orientation of the detector in both flip modes we can use both flip modes to establish the center value along X. Using Circinus X-1 data from Nov. 1996 - Mar. 1997 and May 1997 - September 1997 similar differences in the slopes for the different energy bands as found along Y, is seen. Once again this is consistent with our findings of negative offsets. We interpret the average of the intersections for the different energy bands to be the 'true' center along X, i.e., at 129.7.

7.2. Aligning Layer 3 to Layer 1

To determine the center pixel in layer 3, i.e. determining the true mechanical position of the layer 3 pixels, we used X-ray events with bright narrow spots visible in both layers and shifted the layer 3 image around until we obtained the best spatial correlation with layer 1. Ten events spanning a time interval of more than one ~~a~~ year were examined, and the results are listed in Table 7. The flip mode of the satellite is indicated by the label S for summer and W for winter. The X and Y offsets are values needed to shift the center in layer 3 to obtain maximum spatial correlation. Only correlation coefficients larger than 0.5 are used (? means coefficients smaller than 0.5).

Table 7. Correlation of bright spots seen in layer 1 and layer 3.

Day	Flip mode	X-offset	Y-offset
1996, 12 September	S	- 3.3	0.0
1997, 10 January	W	- 2.7	0.12
1997, 9 February	W	?	0.37
1997, 10 February	W	-2.1	0.5
1997, 24 July	S	- 2.7	?
1997, 31 July	S	- 2.4	1.49
1997, 14 August	S	- 2.7	?
1997, 30 August	S	- 3.1	?
1997, 4 September	S	- 2.3	0.74
1997, 22 November	W	- 2.7	0.0
Average	W/S	- 2.7	0.5

The values found by this method seem to be quite stable for both flip modes in a time interval larger than a year. We believe that these center pixel corrections provides the 'true' location of the layer 3 images relative to layer 1.

In Table 8 the center pixel corrections and the final center values are listed. As can be seen from this table we do not have center values for layer 2 and layer 4, as the correlation study has not been made for these layers.

Table 8. The final center pixel number along X and Y derived from the symmetry point of 'de-PROM'-ed background column (row) sums, Circinus X-1 prediction and correlation of bright spots seen in layer 1 and layer 3.

	X			
Layer	Circinus X-1	Bright spot	Flip S/W	Final Centre
L1	129.7		?	129.7
L3		- 2.7	?	125.5
	Y			
L1	124.6		+/-0.5	124.1 - 125.1
L3		+ 0.5	+/-0.5	127.8 - 128.8

8. Spatial Resolution and Statistical Errors

In order not to smear the image unnecessarily we smooth the final image by 19 times 19 pixels in the 2560 times 2560 matrix, which is about one quart of the pinhole area. However, the spatial resolution is determined by the pinhole size and has to be taken into account in quantitative studies.

To calculate the errors of the flux levels given in our images we keep track of the total number of originally incoming X-ray photons for the specified accumulation time. The relative uncertainty is given by (10), where the uncertainty contribution from background counts is negligible as the sample time for the backgrounds are more than two hours.:

$$\frac{\sigma_X}{n_X} = \frac{\sqrt{\frac{n_T}{t_T} + \frac{n_B}{t_B}}}{\frac{n_T}{t_T} - \frac{n_B}{t_B}} \cong \frac{\sigma_T}{n_X} \qquad (10)$$

where n is counts, t is accumulation time and the subscripts specify X: auroral X rays, T: total X rays and B: background X rays.

9. Some Results

To examine the properness of our image processing we show some results obtained from the PIXIE data set using the procedure described above.

For the 19 April 1996 we have correlated the time development of X-ray fluxes with the radio noise absorption detected at Søndre Strømfjord in Greenland. In Figure 14 the riometer measurements and the X rays in two energy ranges are shown. We have used 75˚ zenith angle in 100 km altitude to draw a circle where the time development of X rays are calculated. The mean X-ray flux for 5 minutes accumulation time every 30 second within the circle is plotted as a function of the center time of accumulation for the two energy ranges. As can be seen the peak intensity of X-ray fluxes correlate very well with the peak of absorption at Søndre Strømfjord. This event is taking place near the time of the flip of the satellite, which means that the temperature in the analogue electronics is above -10˚C. For this event we have provided specific center values and large scale factors following the same scheme as described in the text, but the input for Circinus calibration, correlation between sub-images, and correlation between anodes have been data from April 19, 1996.

From 4 September 1997 we have correlated the electron measurements from NOAA-12 with PIXIE measurements along the satellite trajectory in the morning sector as shown in Figure 15. In the lower panel the PIXIE image from 1200-1205 UT is shown in corrected geomagnetic grid. The NOAA-12 satellite magnetic footprint is marked with solid line. From NOAA-12 we have shown the low electron measurements from 3.6 to 4.9 keV from within the loss cone and electron measurements above 30 keV from within the loss cone (10˚ pitch angle) and outside the loss cone (80˚ pitch angle). The loss cone at 800 km altitude is within pitch angles of ~50˚, which means that the precipitating fluxes that produce X rays are somewhat in between the solid and dashed line in this plot. We see that the low energy X-ray fluxes (2.7-9.4keV) correlates very well with the low energy electron measurements, but it should be noted that these X rays are produced by higher electron energies too. The high energy X rays (7.8-21.2 keV) also correlate very well with the electron measurements above 30 keV

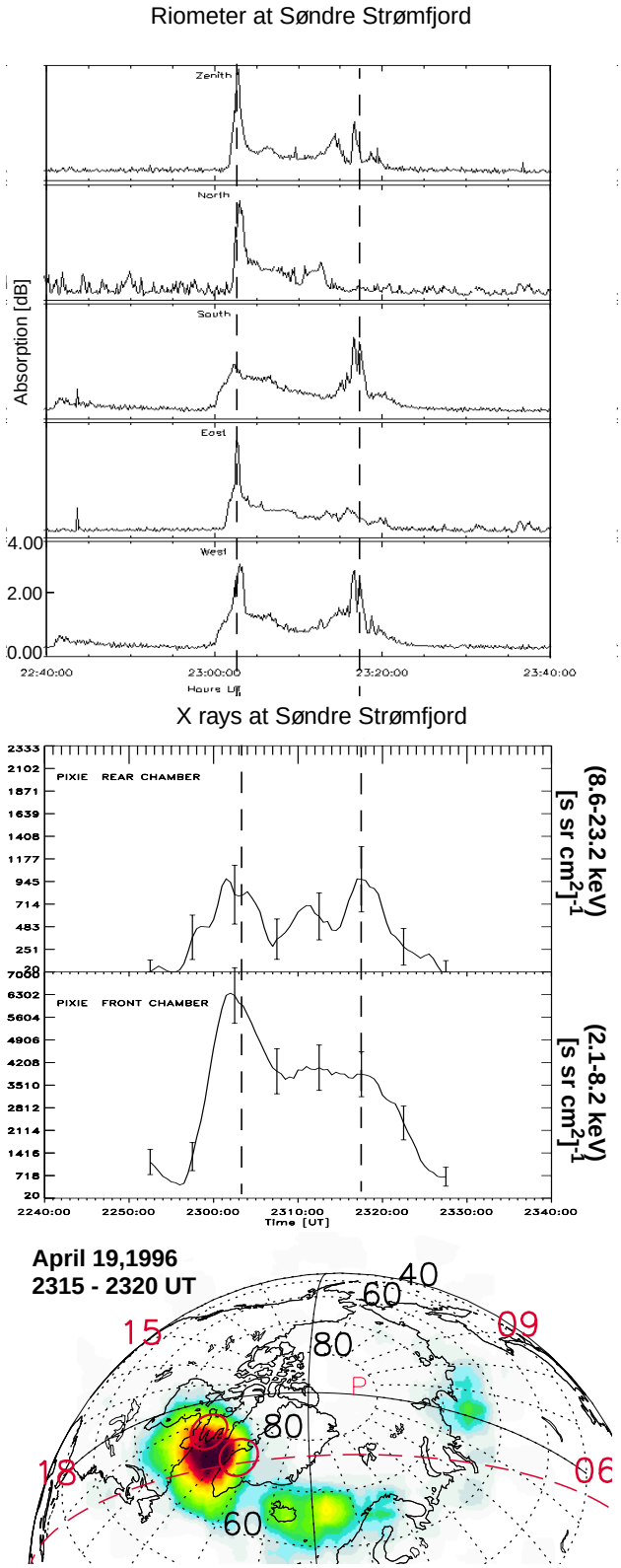

Figure 14. Upper panel: The absorption of radio noise at Søndre Strømfjord 19 April 1996. Second panel: The X rays fluxes within a circle 100 km above Søndre Strømfjord at 70˚ zenith angle, which is shown in red at the PIXIE image in the lower panel (right circle). The grid in the lower panel is corrected geomagnetic coordinates

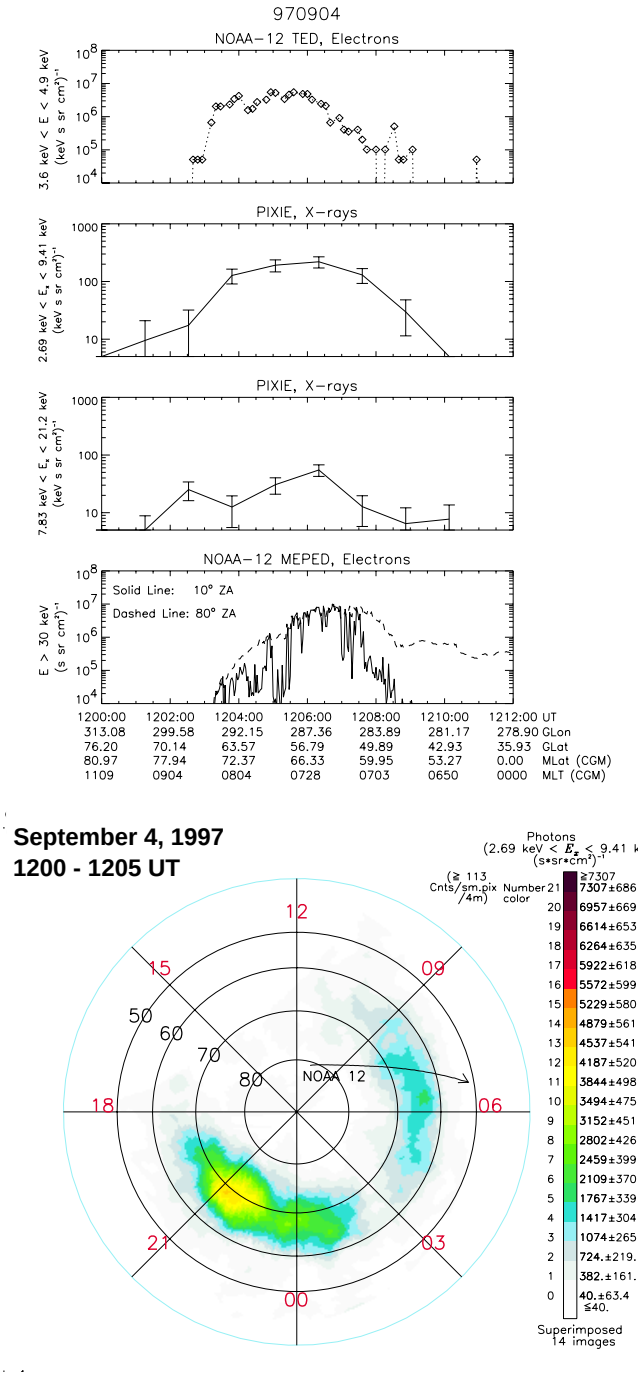

Figure 15. Electron measurements from NOOA 12 and X-ray measurements from PIXIE. First panel: Electrons from 3.6 - 4.9 keV within the loss cone. Second panel: Mean X-ray fluxes from 2.7 to 10.1 keV along the footprint of the NOAA 12 satellite within a circle with diameter 550 km. Third panel: X rays from 9.9 to 19.7 keV within the same circle. Fourth panel: Electrons above 30 keV, solid line at 80˚ pitch angle and dashed line at 10˚ pitch angle. Lower panel: PIXIE image from 1200-1205 UT in corrected magnetic grid. The NOOA 12 satellite trajectory is marked with solid line.

keeping in mind that the precipitating electron flux is somewhere in between the solid and the dashed lines.

Some other results using the data processing method desribed in this paper are already published. A statistical study of global features seen in UV and X rays during substorms [Østgaard et al., 1999] and a case study using PIXIE and GEOTAIL [Håland et al., 1999].

10. Conclusion

By isolating the different processes taking place in the PIXIE camera and provide calibration and correction in a modular step procedure we believe that the spatial resolution for the processed PIXIE image is now restricted basically by the geometry in the camera and the statistically errors due the low count rates of X-ray bremsstrahlung from the ionosphere. We also think the way we have proceeded give us X-ray energy spectra in 5 energy bands (4 from the front chamber and 2 from the rear chamber) which can be used to quantitative studies and calculation of vital parameters as conductivity and electron density in the ionosphere.

Appendix: Analytic Function for Count Rate Correction

First the good event rate has to be corrected due to the electronic dead time and is given by (11).

$$F_C = \frac{1}{1-(R_O \cdot t_P)-(T_O \cdot t_T)} \tag{11}$$

where F_C: Correction factor to obtain the corrected good event rate, R_O: observed good event rate, t_P: processing time for good events = 85 microseconds, T_O: observed throw away rate and t_T: dead time for the read-out throw away events = 15 microseconds.

The provide the next correction we have to estimate the fraction, F_T, for corrected good event count rate to the number of telemetered events. This is analytically given by (12).

$$F_A = \frac{1-\exp(-F_C \cdot 7.36 \cdot 10^{-3})}{F_C \cdot 7.36 \cdot 10^{-3}} \tag{12}$$

As this analytical function does not correspond exactly to the measured corrected count rate an additional gaussian term is added in order to make a best fit (13).

$$G = 0.25 \cdot \exp\left(-\frac{(F_C-110)^2}{2 \cdot 70^2}\right) \tag{13}$$

The total correction fraction, F_T due to the limitation of the buffer size is now given as:

$$F_T = F_A + G \tag{14}$$

and the result is shown in Figure 3. The total dead time correction is provided by multiplying each X-ray event by (15).

$$\frac{1}{F_C \cdot F_T}. \tag{15}$$

The purpose of using this approximate formula is to speed up the processing time by avoiding reading the data files for all the anodes when processing image for just one anode.

Acknowledgments: This study was supported by the Norwegian Research Council (NFR) and by the National Aeronautics and Space Administration under Contract NAS5-30372 at the Lockheed-Martin Advanced Technology Center, Contract NAS5-30369 at the Aerospace Corporation. We acknowledge M. Schulz, D. L. Chenette, W. L. Imhof, S. Petrinec, D. Datlowe, J. Tobin and J. Mobilia at Lockheed-Martin Advanced Technology Center, Palo Alto, California, D. L. McKenzie at the Aerospace Corporation, Los Angeles, California, and J. G. Pronko at Physics Department, University of Nevada, Reno, Nevada for valuable contributions for developing the data processing methods used at the University of Bergen. We want to thank D. Evans for providing particle measurements from the NOAA-12.

References

Berger, M. J., and S. M. Seltzer, Bremsstrahlung in the atmosphere, *J. Atmos. Terr. Phys.*, 34, 85–108, 1972.

Gilvin, P., E. Mathieson, and G. C. Smith, Subdivision of a graded density cathode, *Nuclear Instruments and Methods*, 185, 595–597, 1981.

Håland, S. et al., Magnetospheric and ionospheric response to a substorm: GEOTAIL HEP-LD and Polar PIXIE observations, *J. Geophys. Res.*, 1999. will be published 1999.

Imhof, W. L. et al., The Polar Ionospheric X-ray Imaging Experiment (PIXIE), *Space Sci. Rev.*, 71, 385–408, 1995.

Østgaard, N., J. Stadsnes, J. Bjordal, R. R. Vondrak, S. A. Cummer, D. Chenette, G. K. Parks, M. J. Brittnacher, and D. L. McKenzie, Global scale electron precipitation features seen in UV and X rays during substorms, *J. Geophys. Res.*, 104, 10,191–10,204, 1999.